Passive-Islanding Detection Method Using the Wavelet Packet Transform in Grid-Connected Photovoltaic Systems

Hieu Thanh Do, *Student Member, IEEE*, Xing Zhang, *Senior Member, IEEE*, Ngu Viet Nguyen,
Shan Shou Li, and Tho Thi-Thanh Chu

***Abstract*—In this paper, a new approach in the passive-islanding detection method has been studied for the grid-connected photovoltaic (PV) inverter system using the wavelet packet transform (WPT) and back propagation neural network (BPNN). This proposed method is based on the point of common coupling voltage measurement and processing of this signal with a WPT to find the normalized logarithmic energy entropy. The BPNN is used for decision-making mechanism to avoid threshold. With this technique, the islanding operation is able to detect within 40 ms. In addition, it is effective even when the power supplied by distributed generation and the power consumed by the load is matched. In order to verify the capability of the proposed method, the simulation and experimental results of a 1.2-kW PV inverter by IEC Std. 62116 are provided. The proposed technique can be applied to both single- and multi-PV systems.**

***Index Terms*—Neural networks, nondetection zone (NDZ), passive islanding detection, photovoltaic system, wavelet packet transform.**

I. INTRODUCTION

In the 21st century, the demand of energy is more and more urgent, and the renewable energy is catching the attention of the governments around the world and energy experts in recent years. There are several renewable resources, e.g., solar photovoltaic, wind energy, fuel cell, and geothermal energy in the power system [1]. The power generated from these sources was transferred to the grid, directly or through utility interfaced converters [2]. However, there have been concerns about the rapid dissemination of utility interactive photovoltaic (PV) systems on issues related to safety, power quality, reliability, and stability [3], [4]. One of the most severe safety problems in PV generation is the islanding phenomenon.

According to IEC Std. 62116, islanding is a condition in which a portion of an electric power grid, containing both load and generation, continues to operate isolated from the remainder of the electric power grid [5]. Its drawbacks are concerning to the quality of power, safety for human, and even for protection of power generation. Hence, there are many existing standards, e.g., IEEE Std. 929–2000 [6], IEEE Std. 1547.1–2005 [7], and IEC Std. 62116–2008 [5] that have been established for the grid-connection system. Based on these standards, an islanding detection method should detect the islanding within 2 s of the formation of an island, and the distributed generation (DG) operation must be ceased. Therefore, a fast response and accurate islanding detection method is extremely essential.

Various methods have been proposed to identify the islanding conditions [8]–[15], which can be classified into three categories: active-, passive-, and communication-based methods. Active methods are based on the injection of a small disturbance into the system and analyzing the change in output parameters for islanding detection. Nevertheless, the main limitation of the active methods is that the introduced perturbations will lower the power quality, whereas passive methods require a monitoring of system parameters such as voltage, current, frequency, etc., and the selection of a suitable threshold in order to detect an islanding event. The simplest passive methods are over/under voltage protection (OVP/UVP) and over/under frequency protection (OFP/UFP) [10], [11]. These methods are easy to implement and do no harm the power quality of the system, but they may fail to detect the islanding operation, when the local load closely matches the DG output. Therefore, they are not reliable due to their large inherent nondetection zone (NDZ). Several typical passive techniques are total harmonic distortion (THD) [12], phase jump detection [13], rate of change of frequency (ROCOF) [14], and rate of change of phase angle difference [15].

Most of the DGs have to be integrated with an inverter for grid connection. However, an inverter will always produce some current harmonics in its output current. When the grid is connected, the voltage at the point of common coupling (PCC) is the grid voltage; hence, the harmonics distortion of the PCC voltage is almost zero. On the other hand, when the grid is disconnected, the harmonic currents induced by the inverter will be transmitted to the load, which has much higher impedance than the grid in general. The interaction between the harmonics current and the larger load impedance will generate a larger harmonics voltage. These harmonics are maintained by the filters and embedded with inverter control solutions, and they must be kept below 5% according to IEEE Std. 1547. The magnitude of

---

Manuscript received June 17, 2015; revised September 1, 2015 and October 29, 2015; accepted November 30, 2015. Date of publication December 7, 2015; date of current version May 20, 2016. This work was supported in part by the National Natural Science Foundation of China under Project 51277051 and the National Natural Science Foundation of China under Project 51077034. Recommended for publication by Associate Editor B. Singh.

H. T. Do, X. Zhang, and S. S. Li are with the School of Electrical Engineering and Automation, Hefei University of Technology, Hefei 230009, China (e-mail: 3044929838@qq.com; honglf@ustc.edu.cn; xlisq79@163.com).

N. V. Nguyen and T. T.-T. Chu are with the School of Electrical and Electronic Engineering, Hung Yen University of Technology and Education, Hung Yen 160000, Vietnam (e-mail: ngunguyenviet@yahoo.com; tho.chu.thanh@gmail.com).

Color versions of one or more of the figures in this paper are available online at http://ieeexplore.ieee.org.

Digital Object Identifier 10.1109/TPEL.2015.2506464

the harmonics depends heavily on the grid impedance value, and it will increase in the islanded mode. Thus, using the observation of the voltage and/or current signals in the high-frequency components will provide the best solution to detect the islanding condition [16]–[18].

To decrease NDZ of the passive methods, modern signal-processing tools such as short-time Fourier transform (STFT) [19] and wavelet transform (WT) [20]–[24] have been utilized. Although STFT used a time-frequency window to localize the transients, it did not provide a multiple resolution which was caused by the use of a fixed window size. If the frequency is increased, more and more cycles will appear in the fixed window. Therefore, the individual frequency components are not localized in the window. This issue could be solved by WT. The WT technique works based on the principles of STFT and the multiresolution techniques. The difference between WT and STFT is that the WT uses variable windows for analyzing signals. Unfortunately, the WT only extracts the low-frequency band, so it ignores some useful properties of the high-frequency band, which has meaningful values to reveal islanding condition. Alternatively, the wavelet packet transform (WPT) has been applied which divides the whole time-frequency plane, while the WT can only analyze for low-frequency band [25], [26]. In [27], the WPT was employed for feature extraction (transient high-frequency components) to the direct and quadrature (*d*–*q*-axis) components of the instantaneous 3ϕ apparent powers.

This paper proposed a novel combined algorithm based on WPT signal analysis and back propagation neural network (BPNN), which is applied for islanding detection of the inverter based on DGs. The significant contribution of the proposed method is to provide the reduction of the NDZ region close to zero and avoidance of threshold selection. The method complied with islanding detection tests provided in the IEEE Std. 62116. The critical comparison is presented with the wavelet-based islanding method and the ROCOF method in order to validate the better performances (i.e., faster response, higher reliability, more robustness, etc.) of the proposed method.

This paper is organized as follows. Section II introduces an overview of the WPT and feature extraction. Section III describes the sample system studied. The details of the proposed islanding detection algorithm are presented in Section IV. Section V explains the simulation and experimental results to verify the effectiveness of the proposed method. In Section VI, the results and discussion are presented. Finally, conclusions are drawn in Section VII.

II. THEORY OF THE WPT AND FEATURE EXTRACTION

A. Wavelet Packet Transform

In the orthogonal wavelet decomposition procedure, the generic step splits the approximation coefficients into parts. After splitting, a vector of approximation coefficients and a vector of detail coefficients are obtained, both at a coarser scale. The information lost between two successive approximations is captured in the detail coefficients. Then, the next step consists of splitting the new approximation coefficient vector; successive details are never reanalyzed. However, in the corresponding wavelet packet situation, each detail coefficient vector is also decomposed into two parts using the same approach as in approximation vector split.

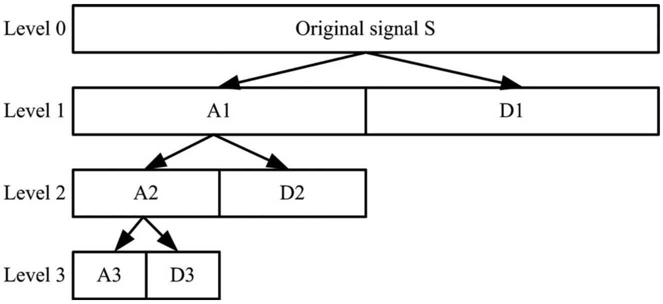

Fig. 1. Structure diagram of three-level wavelet decomposition.

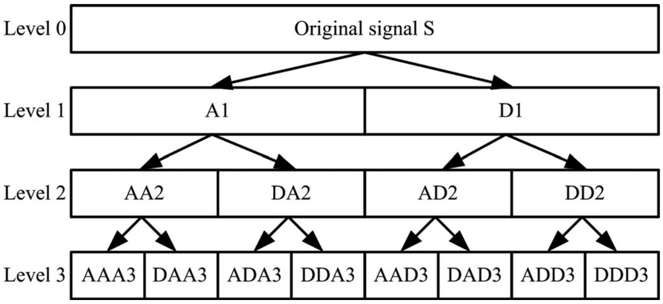

Fig. 2. Structure diagram of three-level WPD.

Based on the above analysis, Figs. 1 and 2 compare three-level wavelet decomposition with wavelet packet decomposition (WPD). It can be seen in Fig. 1 that, in wavelet analysis, only approximations (represented by capital A in the figure) at each resolution level are decomposed to yield approximation and detail information (represented by capital D in the figure) at a higher level. However, in Fig. 2, in the wavelet packet analysis, both the approximation and detail at a certain level are further decomposed into the next level, which means that the wavelet packet analysis can provide a more precise frequency resolution than the wavelet analysis.

The WPT is a generalization of the WT and the wavelet packet function is also a time-frequency function, it can be defined as [28]

$$W_{j,k}^{n}(t) = 2^{\frac{j}{2}} W^{n}\left(2^{j} t - k\right) \tag{1}$$

where the integers *j* and *k* are the index scale and translation operations; *n* is an operation oscillation parameter.

The first two wavelet packet functions expressed as

$$W_{0,0}^{0}(t) = \phi(t) \tag{2}$$

$$W_{0,0}^{1}(t) = \psi(t) \tag{3}$$

where $\phi(t)$ and $\psi(t)$ are the scaling and mother wavelet functions, respectively.

When $n = 2, 3, \ldots,$ the function can be defined by the following recursive relationships:

$$W_{0,0}^{2n}(t) = \sqrt{2}\sum_{k} h(k)\, W_{1,k}^{n}(2t-k) \tag{4}$$

$$W_{0,0}^{2n+1}(t) = \sqrt{2}\sum_{k} g(k)\, W_{1,k}^{n}(2t-k) \tag{5}$$

where $h(k) = 1/\sqrt{2}\,\langle\phi(t),\, \phi(2t-k)\rangle$ and $g(k) = 1/\sqrt{2}\,\langle\psi(t),\, \psi(2t-k)\rangle$ are the filter coefficients of the low-pass and high-pass filters, respectively, and they are orthogonal with the relationship $g(k) = (-1)^k\, h(1-k)$.

The wavelet packet coefficients (WPCs) $S_{j,k}^{n}$ are obtained by the inner product between the signal x(*t*) and the wavelet packet functions $W_{j,k}^{n}$ as

$$S_{j,k}^{n} = \left\langle x, W_{j,k}^{n}\right\rangle = \int_{-\infty}^{+\infty} x(t)\, W_{j,k}^{n}(t)\, dt. \tag{6}$$

B. Feature Extraction Based on Logarithmic Energy Entropy

The information entropy is a measure, which can be used to estimate the complexity of the signal. Due to tool signal frequency components having different performance under different conditions, some frequency components may decay, and some may be enhanced, which would inevitably lead to changes in the tool signal information entropy. Hence, according to the information entropy theory, the calculated information entropy can reflect the distributed situation of energies.

The signal logarithmic energy entropy for each frequency band *n* and *j* level is calculated as

$$E_{j,n} = \sum_{i=1}^{N} \log\left[\left(S_{j,k}^{n}(i)\right)\right]^2 \tag{7}$$

where *N* is the number of sampling point, $S_{j,k}^{n}$ is the WPCs at the *n*th frequency band on the *j*th level, $n = 2^j$-1.

Also, for better demonstration of the distributed situation of the total signal logarithmic energy entropy in each frequency band, the normalized logarithmic energy entropy (NLEE) value is given by

$$E_n = \frac{E_{j,n}}{\sum_{n=0}^{2^j-1} E_{j,n}}. \tag{8}$$

III. SAMPLE SYSTEM STUDIED

A. System Studied

Fig. 3 shows a single-phase circuit which is the same as the testing diagram defined in IEC Std. 62116-2008. As depicted in Fig. 3(a), the test circuit consists of a PV array, a full-bridge inverter, a local load, a circuit breaker, and the utility grid. The inverter with the local load is connected to the utility grid through the closed circuit breaker SW1. When the circuit breaker SW1 is closed, the system is operating the under grid-connected mode. On the other hand, once the utility grid is disconnected, the PV inverter and the *RLC* load will operate under the islanding mode. The block diagram of the inverter controller is shown in Fig. 3(b).

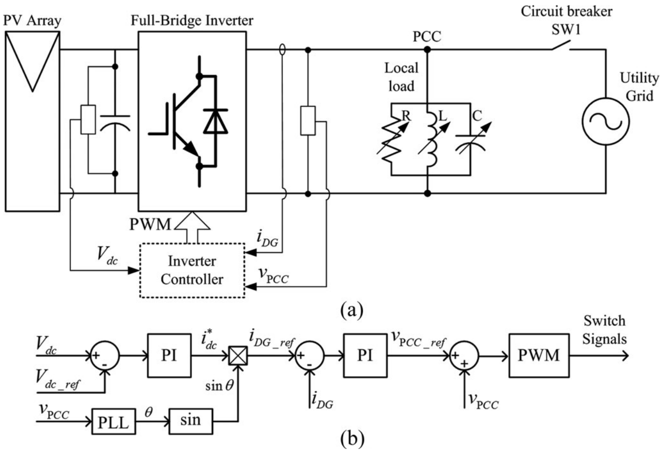

Fig. 3. (a) Typical single-phase PV inverter system configuration. (b) Block diagram of the inverter controller.

The control unit works as follows: the PCC voltage $V_{\rm PCC}$ is measured at the PCC point and fed to the phase-locked loop to determine the phase angle θ. In addition, the dc-link voltage $V_{\rm dc}$ is compared to the reference dc voltage $V_{\rm dc\_ref}$, and the difference between them were used as an input to the proportional-integral (PI) controller. The output of the PI controller is the reference current of the dc capacitor $i_{\rm dc}^{*}$. The reference DG current $i_{\rm DG\_ref}$ is the product of $i_{\rm dc}^{*}$ and sinθ; and it is compared to the DG output current $i_{\rm DG}$. Finally, in order to control the inverter-based DG switches, the sum of the reference PCC voltage $V_{\rm PCC\_ref}$ and the PCC voltage $V_{\rm PCC}$ were used as input to the pulse with modulation.

B. Events Used in the Training System

The initial sample studied is shown in Fig. 3. The possible situations of the islanding and nonislanding conditions studied are given as follows:

1) trip the utility breaker to island the DG along with active power mismatch from -40% to 40%;
2) trip the utility breaker to island the DG along with reactive power mismatch from -40% to 40%;
3) trip the utility breaker to island the DG along with active power mismatch from -10% to 10% and the reactive power mismatch from -10% to 10%;
4) sudden load change at PCC;
5) various load quality factors;
6) capacitor bank switching.

In order to design and evaluate the proposed method, 240 different islanding and nonislanding events are simulated. There are 120 islanding and 120 nonislanding events. More details about cases tested are summarized in Table I.

IV. PROPOSED ISLANDING DETECTION ALGORITHM

The details of the proposed method, i.e., the concept, feature extraction, pattern recognition, and structure of the proposed algorithm are presented in this section.

TABLE I
GENERATED DATASET

Cases	Case Description	No. of Data Samples
Islanding	Island with ±40% of active power mismatch	36
	Island with ±40% of reactive power mismatch	36
	Island with ±10% of active power mismatch and ±10% of reactive power mismatch	48
Nonislanding	Load switching	40
	Various load quality factors	40
	Capacitor bank switching	40

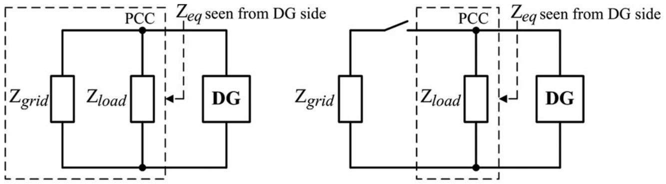

(a) (b)

Fig. 4. Single-phase equivalent impedance has seen from the DG side. (a) Normal operation. (b) Islanding operation.

A. Concept of the Proposed Method

During the process of converting sustainable energy into electricity, inverter-based DGs produce the harmonic components in the DG output voltage and the current at the PCC. Because of the wide use of power electronics-related equipment and their nonlinear input characteristics [29], [30], the harmonic exists in a huge range. Beside, with the existence of high-frequency switching, dead time, control delays, nonlinear inductors, and direct current link voltage ripple, the inverter will produce a large amount of current harmonics [31]. Rigorous analysis of the harmonic distortion which is produced by nonlinear devices is extremely complex. Therefore, an approximate analysis is used to simplify the computation in which nonlinear loads are considered to be sources of harmonic currents [29]. Using a current sources approximation, the harmonic voltage at the PCC point is a function of the harmonic current and the impedance of the grid at each harmonic frequency.

Fig. 4 illustrates the equivalent impedance Z_{eq} that can be seen from the DG side under normal and islanding operation. It can be seen that at the instant of islanding, the equivalent impedance suddenly increases from $(Z_{\text{load}}Z_{\text{grid}})/(Z_{\text{load}} + Z_{\text{grid}})$ to Z_{load}. Therefore, the magnitude of the harmonics depends heavily on the grid impedance value and will increase in the islanding mode of operation. Hence, the changed spectral occurs in the high-frequency components of the PCC voltage signal which has been selected to detect the islanding condition.

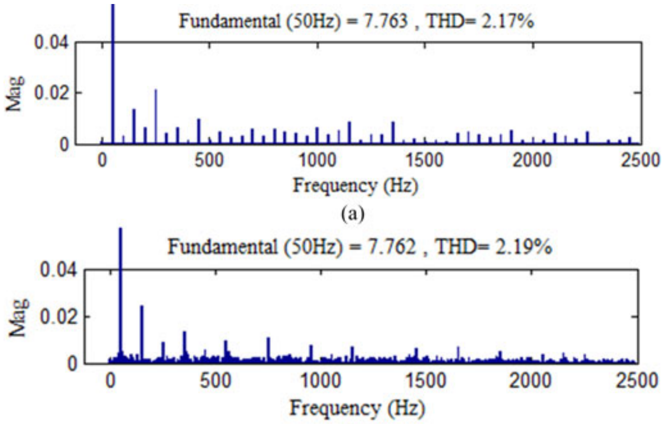

(a)

(b)

Fig. 5. Harmonic spectrum of the inverter output current: (a) before islanding and (b) after islanding.

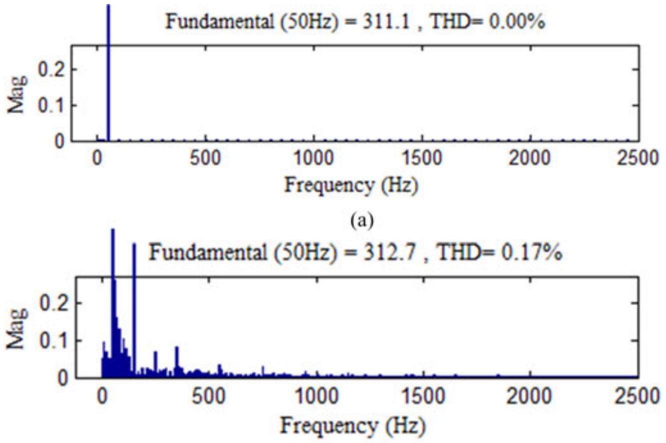

(a)

(b)

Fig. 6. Harmonic spectrum of the PCC voltage: (a) before islanding and (b) after islanding.

Figs. 5 and 6 illustrate the harmonic spectral of the inverter output current and the PCC voltage in case of zero active and reactive power mismatches, respectively. From Fig. 5, it can be clearly seen that before and after the islanding event occurs, the variation of the THD of the inverter output current is negligible, whereas during the grid-connected operation, the PCC voltage THD is ≈0% and it increases during the islanding operation, reaching to ≈0.17%, as shown in Fig. 6. This is due to the variation of the high-frequency impedance between islanding and grid-connected condition.

In order to solve the above problem, the WPT technique is used in this paper to examine the changed spectral occurring in the high-frequency components of the PCC voltage signal due to islanding.

B. Feature Extraction

The purpose of the feature extraction is to identify specific signature of the PCC voltage signal that will help in distinguishing between islanding and nonislanding condition.

Fig. 7 shows the PCC voltage and the inverter output current waveforms, which was acquired when the power is supplied by the PV inverter, and the power consumed by load is balanced. The islanding scenario is created at 0.3 s (3000th point). It can be seen from Fig. 7 that once the islanding occurs, the high-frequency components of the PCC voltage increase significantly.

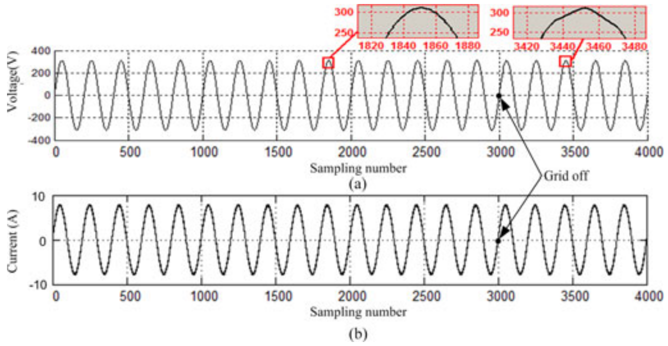

Fig. 7. PCC voltage and inverter output current waveforms when the power of the inverter and load are matched.

TABLE II
FREQUENCY BAND OF EACH LEVEL

WPD level	Frequency band (Hz)
1	0–2500, 2500–5000
2	0–625, 625–1250, 1250–2500, 2500–5000
3	0–39.0625, 39.0625–78.125, 78.125–156.25, 156.25–312.5, 312.5–625, 625–1250, 1250–2500, 2500–5000

The signal sampling frequency is 10 kHz; sampling number is 200 points for each period. On the other hand, the simulation total time is 0.4 s, so the sampling number is 4000 points.

Different wavelet basic functions having different orders can affect the results. In fact, using a proper mother wavelet has an important role in the analysis. Daubechie's wavelet family is one of the most suitable wavelet families in analyzing power system transients and islanding detection as investigated in [17], [32]–[34]. In the proposed study, the PCC voltage signal is decomposed by WPT which chooses Daubechie's 5 (db5) and the layer of decomposition are 3. Therefore, the PCC voltage signal is decomposed into eight frequency bands. Table II summarizes the frequency bands of each level which have been decomposed. According to IEEE 519–1992 Std., the DG systems as PV inverter output current should have a low distortion level. The total current distortion should be less than 5% of the fundamental current [35]. Odd harmonics including third, fifth, seventh, and ninth orders are the main harmonics in the inverter output current. Therefore, the frequency range of high-frequency components of the PCC voltage waveform generally exists in a range of 75–450 Hz. This frequency range is found in band 2 (39.0625–78.125 Hz), band 3 (78.125–156.25 Hz), band 4 (156.25–312.5 Hz), and band 5 (312.5–625 Hz). Hence, the previously mentioned bands are used as the most suitable decomposition frequency band to compute NLEE of the PCC voltage in this study.

Fig. 8 illustrates the WPC of each frequency band. In Fig. 8, *x*- and *y*-axes are the sampling number and the amplitude of the WPC, respectively. The amplitude of the WPCs during islanding condition changes significantly in comparison when the grid is connected, especially in the nodes (3, 1), (3, 2), (3, 3), and (3, 4). Then, the NLEE value of these nodes with the worst detection

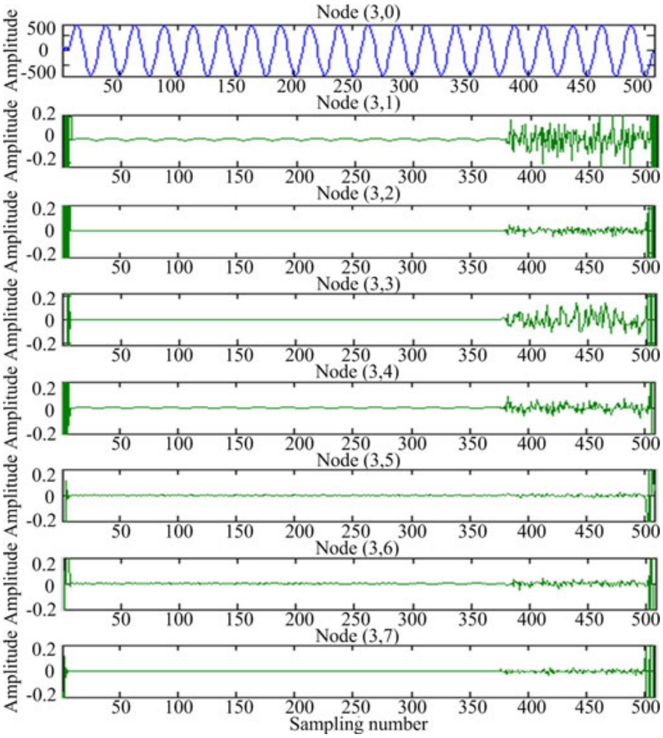

Fig. 8. WPCs of the PCC voltage signal at level 3 with "db5" wavelet.

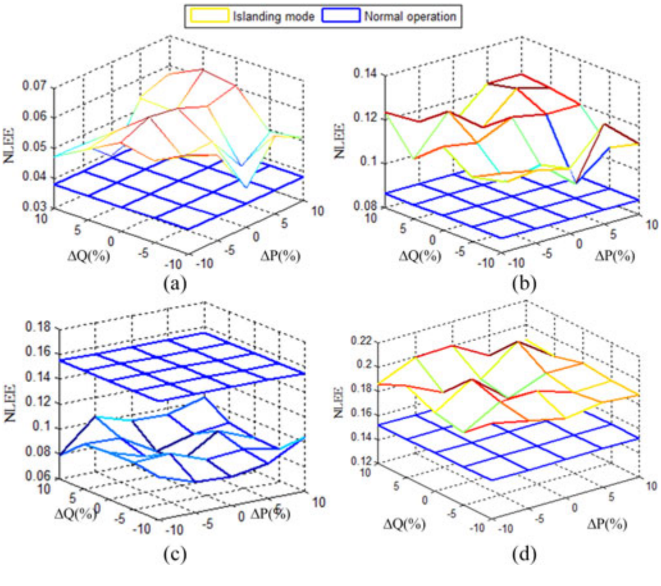

Fig. 9. NLEE of different frequency bands for islanding mode and normal operation: (a) node (3,1), (b) node (3,2), (c) node (3,3), and (d) node (3,4).

conditions (as given in Table IV) will be calculated. The NLEE values of the nodes (3, 1), (3, 2), (3, 3), and (3, 4) are E1, E2, E3, and E4, respectively. Fig. 9 shows all of selected indices in various islanding and normal operation events, which are used to build the classification model of the islanding detection relay. It can be seen that the NLEE values of each node considerably change between islanding mode and normal operation. Hence, E1, E2, E3, and E4 are selected as a feature vector in this study.

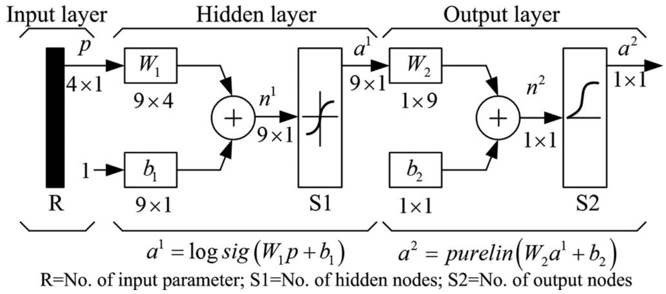

Fig. 10. BPNN structure of the proposed method.

C. Pattern Recognition

According to the results in Section IV-B, the values E1, E2, E3, and E4 for various conditions used a threshold value between the islanding mode and the normal operation. Therefore, the distinguishing between islanding and nonislanding condition can be an example, and the value 0.12 can be considered as the threshold value. If the value of E3 is lower than 0.12, the islanding condition is detected. The nonislanding condition is detected if the value of E3 is higher than 0.12. This is simple example, and the threshold to distinguish the islanding condition can be easily determined. However, working conditions have no obvious limit and more complex, so they cannot be distinguished strictly. Hence, BPNN approach was adopted to determine the islanding condition.

The BPNN structure is shown in Fig. 10. The network used in this case contains three layers namely the input layer, the hidden layer, and the output layer. The node number of the input layer and the output layer are the same with the number of the feature vectors and the classifications of the study. Thus, the nodes of the input layer and the output layer are 4 and 1, respectively. Moreover, during the design of BPNN, the key is to determine the number of nodes in the hidden layer. Too few hidden nodes, the functionality of the network will be poor, while too many hidden nodes will cause the network to over-fit the data. The selection node number of the hidden layer is determined based on experience and usage. So, the node number of the hidden layer was determined by the trial and error method in this study. Based on this method, at the hidden layer with nine nodes, target mean square error (MSE) of 0.0001 was achieved. When the node number was increased more than 9, it causes an unrealistic result and increases the MSE values. Hence, the nodes of the hidden layer are determined to 9. So, the network structure of BPNN is 4–9–1. In addition, the function of *logsig* is used in the hidden layer and the function *purelin* is used in the output layer.

D. Structure of the Proposed Algorithm

Fig. 11 illustrates the architecture of the proposed method. It consists of three modules. The first is the input which includes four mentioned signals. The second is the BPNN, and the final is the tripping unit; the trip signal is connected to control the relay RL as shown in Fig. 12. The value of the BPNN output is either high to indicate islanding occurrence and the trip signal is set to “1” or low to indicate that the DG is still connected to the grid and the trip signal is set to “0.”

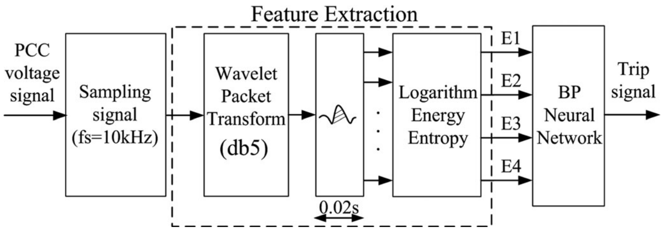

Fig. 11. Architecture of the proposed method.

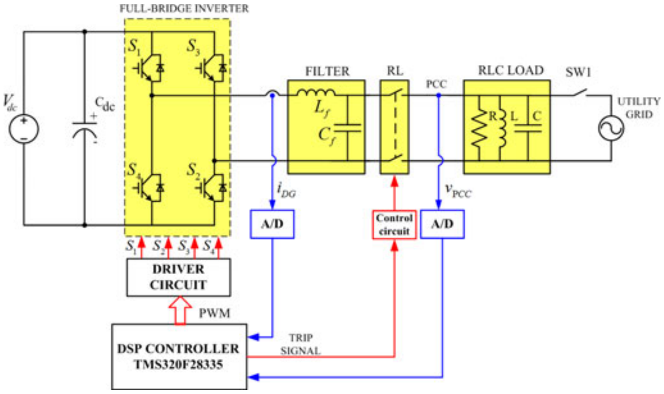

Fig. 12. Block diagram of the system setup used for simulation and experiment.

The working principle of proposed method is as follows. First, one cycle data of the PCC voltage is collected at the end of each cycle. The sampling frequency used is 10 kHz, one cycle includes 200 samples. Second, the PCC voltage is decomposed to eight different bands (level = 3) using multiresolution wavelet packets and the NLEE value for each frequency band will be calculated using a window of 0.02 s. Finally, the NLEE values of the PCC voltage (E1, E2, E3, and E4) are used to feed the BPNN for training and testing. The determination islanding happened or did not happen was performed by the training assistance of BPNN. In the case of islanding, the trip signal is sent to the circuit breaker at the PCC to disconnect DG from the grid.

V. SIMULATION AND EXPERIMENTAL RESULTS

A. Simulation Results

In order to verify the viability of the proposed islanding detection method, a single-phase grid-connected PV inverter system has been built. The block diagram of the system setup shown in Fig. 12 is simulated in MALAB/SIMULINK software. As shown in Fig. 12, the block diagram is comprised of five parts: 1) a dc-link voltage V_{dc} from renewable energy sources; 2) a full-bridge inverter (S_1 to S_4); 3) an *LC* output filter L_f and C_f; 4) an *RLC* load; and 5) a utility grid. The main parameters used in the simulation are listed in Table III. Initially, the inverter with a local load is connected to the power grid via a closed-circuit breaker SW1, and then, the circuit breaker SW1 is opened in order to form an islanding condition.

TABLE III
SYSTEM PARAMETERS FOR SIMULATION AND EXPERIMENT

Parameter	Value
DC voltage V_{dc}	400 V
Rate power of inverter	1200 W
Filter inductor L_f	5 mH
Filter Capacitor C_f	3 μF
Resistance load	40.333 Ω
Inductance load	128.4 mH
Capacitance load	78.919 μF
Quality factor	1
Nominal grid voltage	220 V
Grid frequency	50 Hz

TABLE IV
LOAD IMBALANCE FOR TEST CONDITION

	% change active load from nominal				
% change reactive load from nominal	−10, +10	−5, +10	0, +10	+5, +10	+10, +10
	−10, +5	−5, +5	0, +5	+5, +5	+10, +5
	−10, 0	−5, 0		+5, 0	+10, 0
	−10, −5	−5, −5	0, −5	+5, −5	+10, −5
	−10, −10	−5, −10	0, −10	+5, −10	+10, −10

For brevity, only the results of the islanding condition and the effect of the active and reactive power mismatches will be presented. According to IEC Std. 62116, the performance of the proposed technique was verified with various conditions as shown in Table IV. Under these conditions, the power flows (ΔP, ΔQ) were changed from −10% to +10% of the inverter output power with 5% steps, which is very difficult to detect the island mode. For the other tested conditions, the circuit breaker SW1 will be opened at $t = 0.3$ s and the inverter along with the local load is isolated from the power grid and the islanding status occurs.

Fig. 13 shows the variation peak amplitude and the frequency of the PCC voltage when ΔQ is set to 0% and ΔP is changed among −10% to +10%. It can be seen obviously that after islanding, the peak amplitude remains within the acceptable range and the frequency deviation is negligible. Similar results for the effective peak amplitude and the frequency of the PCC voltage are depicted in Fig. 14, when ΔP is set to 0% and ΔQ is changed among −10% to +10%. It is shown that after islanding, the peak amplitude is negligible and the frequency deviation remains in the acceptable range. Thus, the results illustrated that the passive method based on OVP/UVP and OFP/UFP relay failed to detect the islanding mode with the conditions in Table IV. Finally, the trip signal is presented in Fig. 15.

When the power of the local load is designed to match the generation power of the PV inverter, the islanding detection is extremely difficult; thus, according to IEC Std. 62116, three typical worst-case studies were considered to prove the effectiveness of the proposed algorithm as follows.

Case A: Inverter output power is equal 100%, and ΔP is set to 0%; ΔQ is set to −5% of inverter output power.

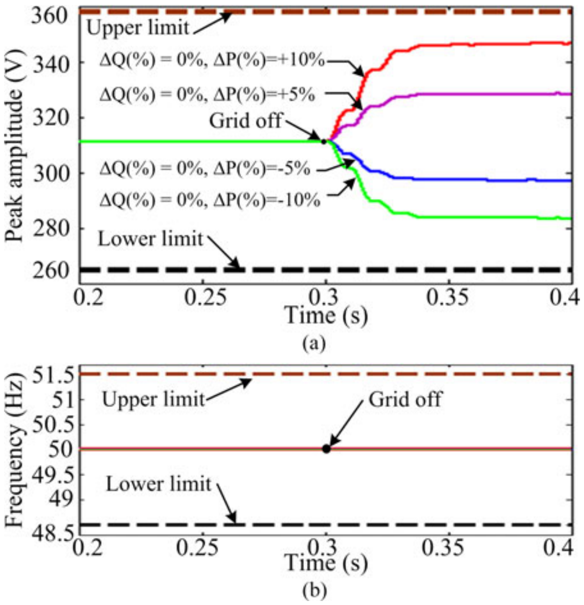

Fig. 13. Effective PCC voltage waveform for the islanding mode in active power mismatch. (a) Peak amplitude. (b) Frequency.

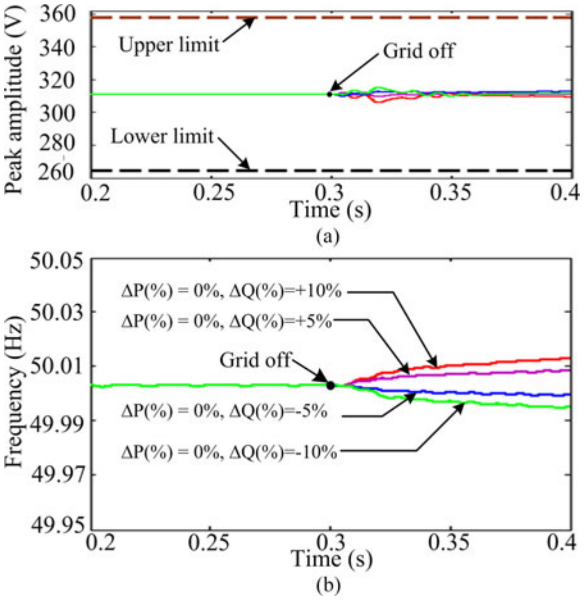

Fig. 14. Effective PCC voltage waveform for the islanding mode in reactive power mismatch. (a) Peak amplitude. (b) Frequency.

Case B: Inverter output power is equal 66%, and ΔP is set to 0%; ΔQ is set to +1% of inverter output power.

Case C: Inverter output power is equal 33%, and ΔP is set to 0%; ΔQ is set to +1% of inverter output power.

Fig. 16 shows the simulation results by the proposed method under case A. Fig. 16(a)–(d) shows the PCC voltage, inverter current, load current, and grid current, respectively, while Fig. 16(e) and (f) illustrates the corresponding value of the BPNN output and the trip signal. It can be observed from Fig. 16(d) that before the islanding happens, the grid current

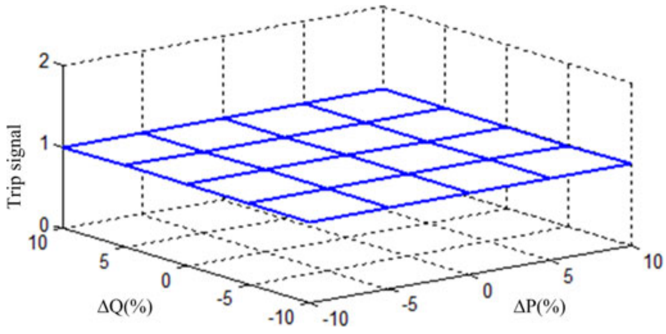

Fig. 15. Trip signal for the islanding mode in various conditions.

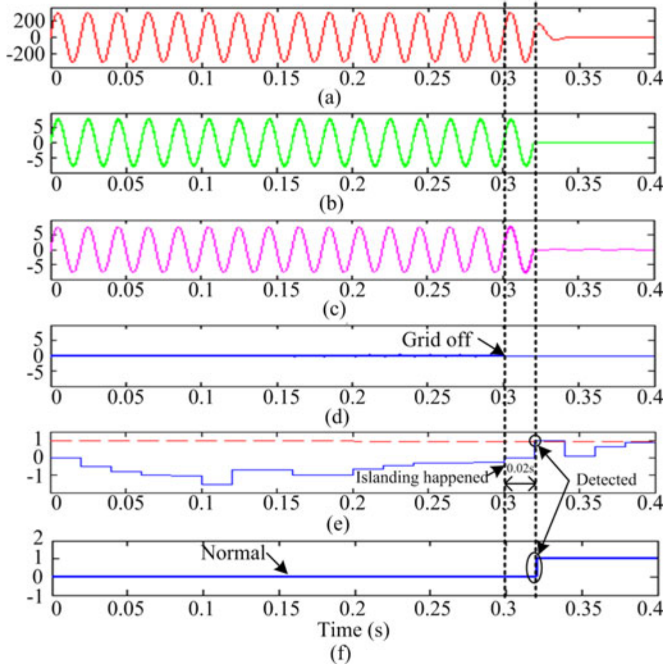

Fig. 16. Simulated islanding test results in case A.

is close to zero because the active consumption power of the local load is designed to match the PV inverter output active power. In Fig. 16(e), it can be seen that during normal state, the BPNN output value remains lower than 1 for most of the simulation time. Therefore, the trip signal is set to “0.” When the circuit breaker SW1 opens at $t = 0.3$ s, then the islanding happens, and the grid current drops to zero. The BPNN output value increases after the islanding occur; exceeding 1 at $t = 0.32$ s and the trip signal is set to “1.” The waveform of the inverter output current and the load current also drop to zero after detect the islanding status. The detection time of the islanding operation is 0.02 s. This result proved that the proposed method could effectively detect the islanding phenomenon for case A.

Figs. 17 and 18 show the same results as Fig. 16 in cases B and C, respectively. These figures show that at $t = 0.3$ s, the grid is disconnected and the grid current drops to zero. These cases could also effectively detect the islanding phenomenon and the detection time of 0.02 s. In fact, the proposed method is highly effective and reliable in decision making for islanding detection with active and reactive power mismatch at the lower end.

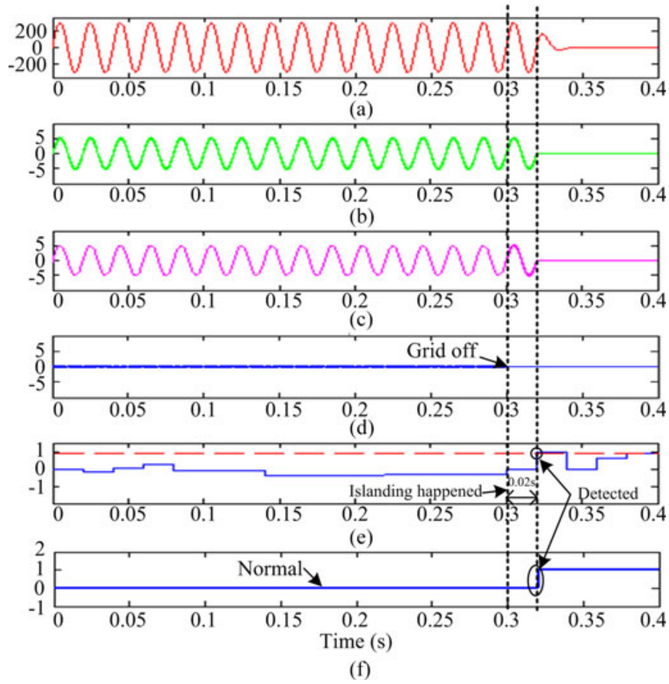

Fig. 17. Simulated islanding test results in case B.

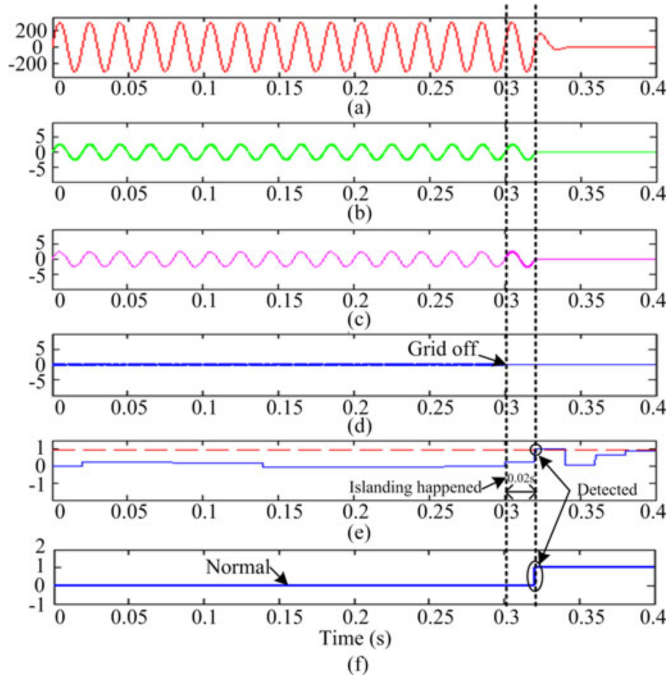

Fig. 18. Simulated islanding test results in case C.

B. Experimental Results

The hardware configuration with a 1.2-kW single-phase grid-connected PV inverter system has been constructed in software

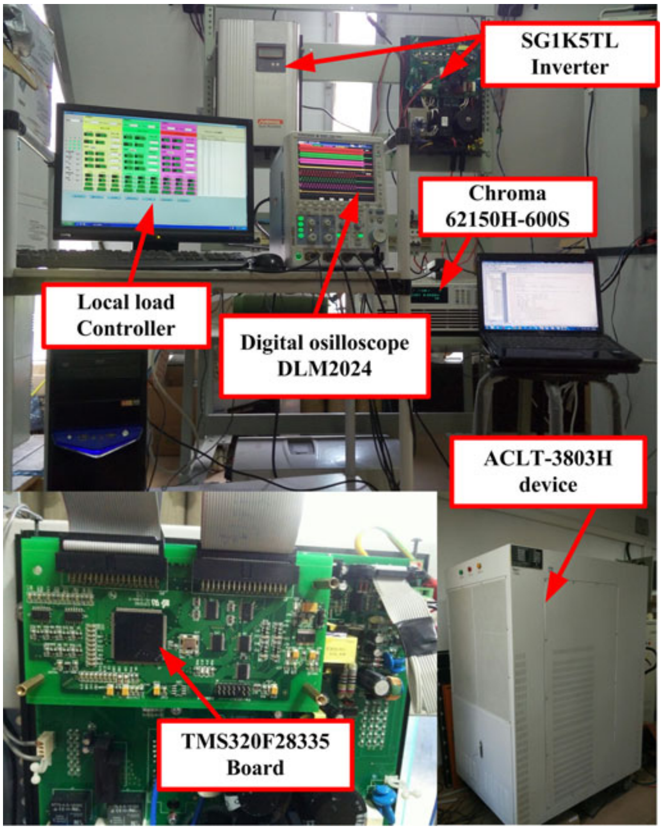

Fig. 19. Photograph of the experimental setup to test the proposed method.

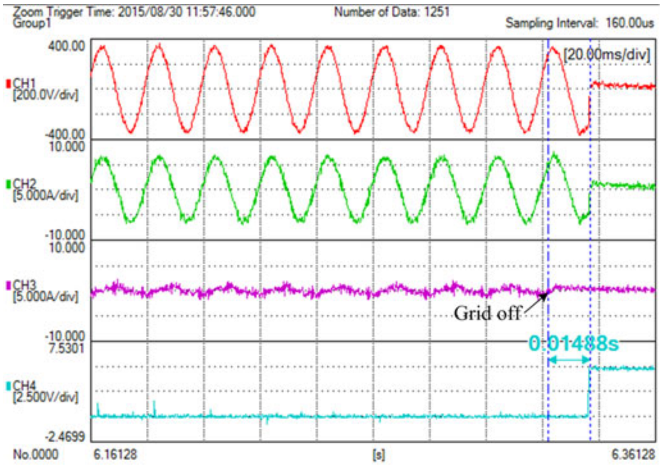

Fig. 20. Experimental results of islanding detection by the proposed method in case A.

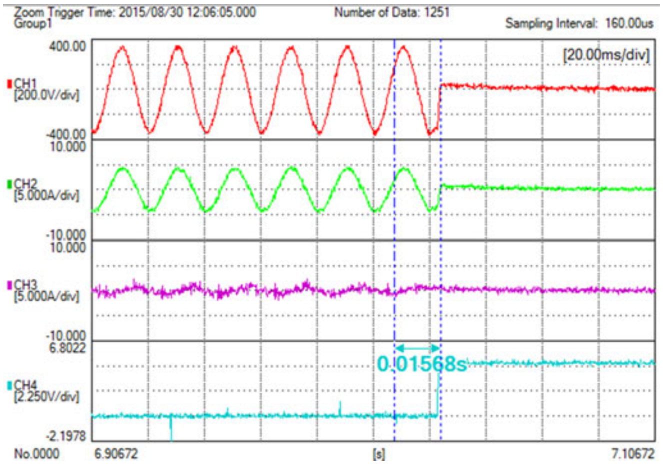

Fig. 21. Experimental results of islanding detection by the proposed method in case B.

and hardware as illustrated in Fig. 12. The software part was realized by using 32-bit digital signal processor (DSP) TMS320F28335 board, including the control of the PV inverter with the necessary islanding algorithm. The outputs of the software part consist of signals for the power devices and the trip signal to control a relay *RL* (antiislanding protection). Furthermore, the PCC voltage v_{PCC} and the inverter output current i_{DG} were measured using voltage and current sensors, and fed to the analog-to-digital converter ports of the DSP board. These voltages and currents were also collected to the digital oscilloscope using the four-channel YOKOGAWA DLM2024 device. The hardware part was composed of the following.

1) The dc-link voltage source was realized by using the Chroma 62150H-600S programmable dc power supply.
2) *Full-bridge inverter:* The inverter used was SG1K5TL, which is manufactured by Sungrow Power Supply Co., Ltd.
3) *The local load:* ACLT-3803H antiislanding test device, which is manufactured by Beijing QunLing Energy Resources Technology Co., is adopted in the experiment. Through the serial port communication, the antiislanding test device may set local load for different values, and the reliability of the proposed islanding detection methods can be verified.
4) *Grid:* The grid is obtained from a 1ϕ, 220 V/50 Hz.

Fig. 19 shows a photograph of the experimental setup for testing the proposed method. The parameter values used in the experiments are the same as the ones used for simulation, as listed in Table III.

The three cases, in the previously mentioned simulation, were verified by the hardware experiment. The obtained experimental results are shown in Figs. 20–22, where channel CH1 corresponds to the measured voltage waveform at the PCC, channel CH2 shows the inverter output current waveform, channel CH3 shows the grid current waveform, and channel CH4 shows the trip signal, which simulates the grid disconnection.

Responses of the system for cases A, B, and C are shown in Figs. 20, 21, and 22, respectively. In these cases, the PV inverter is working at 100%, 66%, and 33% of its rated power. From Figs. 20–22, when the grid is connected, the grid current is close to zero because in these cases the active consumption power of the local load is designed to match the PV inverter output active power, whereas, once the islanding occurs, the grid current is immediately equal to zero. The instant islanding is formed which can be identified at the moment the grid current is dropped to zero.

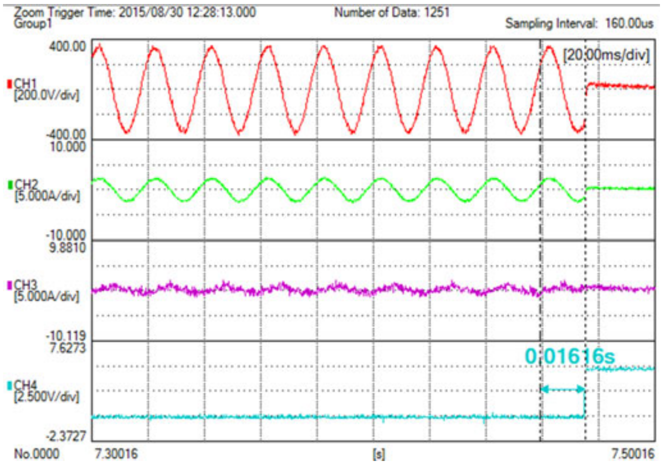

Fig. 22. Experimental results of islanding detection by the proposed method in case C.

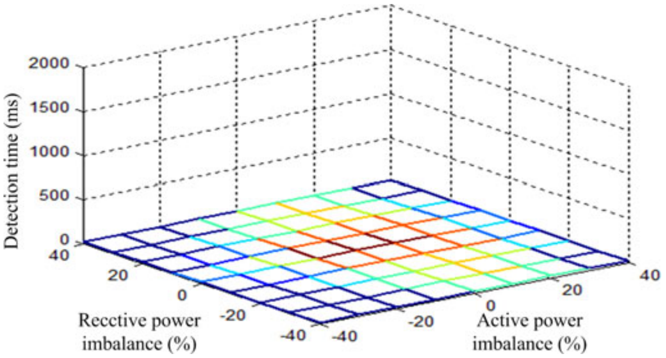

Fig. 23. Variation of islanding detection times of the proposed method under varying active and reactive power imbalance.

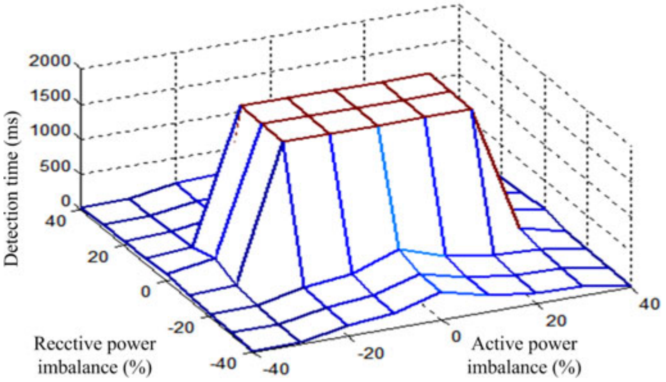

Fig. 24. Variation of islanding detection times of OVP/UVP and OFP/UFP relay under varying active and reactive power imbalance.

The results indicated that after the islanding is detected, the PV inverter is stopped immediately and the inverter output current and the load current are zero as well. The needed times for the detection of the islanding phenomenon in Cases A, B, and C are 14.88, 15.68, and 16.16 ms, respectively, which are less than 2 s in the STD. IEC 62116.

Based on the all experimental results, it is confirmed that the proposed method could detect the islanding status within two cycles of the PCC voltage, indicating that the proposed technique is able to detect the islanding quickly. In addition, the experimental results are consistent with the simulation results.

VI. Results and Discussion

A. *NDZ of the Proposed Method*

The effectiveness of the islanding detection method is usually represented by the NDZ. In order to evaluate the NDZ region, the performance of the proposed method is investigated with respect to active and reactive power mismatches ranging from −40% to 40% during the islanding. Large-power mismatch cases are not considered here because they can be easily detected by conventional detection methods [10]. The simulation detection times of all relays for the 81 islanding cases were recorded. The results are presented in the three-dimensional (3-D) surface graph, as shown in Fig. 23, representing the active power imbalance (%), reactive power imbalance (%), and relay detection times in the x-, y-, and z-axes of the graph, respectively. The events of those that did not detect the islanding within 2 s were considered as nondetected. Figs. 23 and 24 illustrate the detection times of the islanding detection method by the proposed method, and OVP/ UVP and OFP/ UFP relay, respectively.

The NDZ region can be found by chopping the surfaces using a horizontal plane at the detection time of interest. These figures are drawn for a 2-s time frame for islanding detection and, therefore, the plateau on the 3-D plot represents the NDZ of each relay in the *PQ* plane. The observed results show that the proposed method has a zero NDZ, while the OVP/ UVP and OFP/ UFP relays show very poor performance with higher detection times, and a considerably large NDZ, as can be seen in Fig. 24.

B. *Comparison of Detection Time*

The speed of detection is one of the advantages in the proposed islanding detection method. The proposed method works with one-cycle data, i.e., the data used to calculate the NLEE are updated each cycle. For most cases, if the DG is islanded at any instant of the cycle, it will be detected at the end of that cycle. However, when the islanding occurs near the end of cycle, the islanding may be detected in the next cycle. Consequently, the detection time in this method is less than two cycles, considering the instance of the islanding occurrence in a cycle and the required computation time.

The response times of the proposed method, the wavelet-based islanding method in [23], and ROCOF relay in [14] with respect to active power mismatch ranging from 0% to 90% during islanding are shown in Fig. 25 for comparison. The observed results show that the operating time is inversely proportional to the active power mismatch in case of ROCOF. When the active power mismatch is high, the response time reduce drastically, and the reverse happens when the active power mismatch is at the lower end. Nevertheless, significant improvement has been observed in this study and the wavelet-based

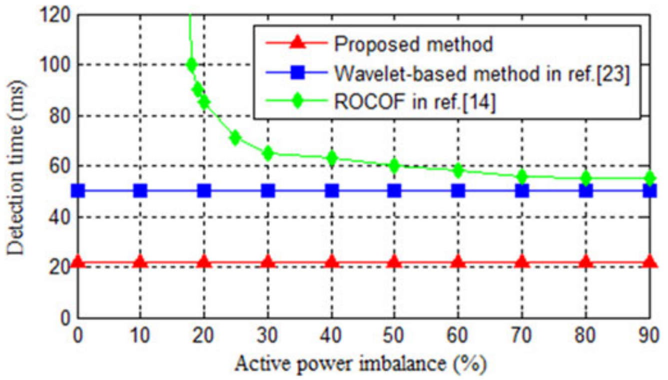

Fig. 25. Response time of the proposed method, the wavelet-based method in [23] and ROCOF relay in [14].

TABLE V
CLASSIFICATION RESULTS OF THE PROPOSED METHOD

	Event	Total cases	Correct detection	Classification accuracy (%)
Training	Islanding	50	49	98
	Nonislanding	50	50	100
	Total	100	99	99
Testing	Islanding	70	68	97.14
	Nonislanding	70	70	100
	Total	140	138	98.57

islanding method in [23]. It is found that the detection time is almost constant for different ranges of the active power mismatch. Furthermore, the most valuable contribution of the method in this study is the average detection time which is only 22 ms. Besides, in the case of ROCOF, relay is unable to detect islanding conditions below 15% of the active power mismatch, whereas the proposed method and the solution in [23] are able to perform the task as shown in Fig. 25.

C. Overall Performance of the Proposed Method

A total of 240 events (including 120 islanding and 120 nonislanding) are generated under the different operating conditions discussed in Section III-B. Moreover, 50 islanding and 50 nonislanding events are used for the training purpose, and the remaining events are used for the testing purpose. Nevertheless, due to the random nature of the experiment, slight differences may occur between the performance of the BPNN model for different training and testing dataset. Therefore, the training and testing process was repeated ten times by randomly selecting the training and testing dataset from the above events.

Table V shows the results of BPNN-based classification. The classification accuracy of the proposed method is compared with other methods in [20] and [21]. The method based on the WT presented in [20] could obtain 96.43% accuracy by using the fourth level of the discrete wavelet transform of both voltage and current signals. A neuro-wavelet-based islanding detection technique in multiple DGs was proposed in [21]. The simulation result shows the maximum accuracy of 97.77%. However, the overall accuracy of the proposed technique in this paper is estimated to be 98.57% using only voltage and three levels of the WPT. It is verified that the proposed technique works effectively and is more accurate than the presented methods in [20] and [21].

TABLE VI
CLASSIFICATION RESULTS OF WITHOUT AND WITH NOISE

Event	Total cases	Correct detection	Classification accuracy (%)
Features without noise			
Islanding	15	0	100
Nonislanding	5	0	100
Features with SNR 20-dB			
Islanding	15	0	100
Nonislanding	15	0	100

D. Performance Under the Effect of the Signal Noise

This section focuses on the effect of the signal noise on the classification accuracy. The BPNN classifier designed for the islanding relay was not trained with noisy data. In order to investigate the effect of the noise on the islanding accuracy, the designed classifier was tested with a set of noisy data. Table VI depicts the classification accuracy for data with and without noise. The classification accuracy is 100% for 30 test cases of different conditions for features without noise and with 20-dB signal-to-noise ratio (SNR). Then, the proposed method is found to be accurate and robust for islanding detection.

VII. CONCLUSION

In this paper, a new passive-islanding detection method for PV systems which can detect islanding condition from local measurements of the PCC voltage signal is presented. The simulation and experimental results indicate that the proposed scheme is capable of detecting islanding events even under the worst-case scenario, where the inverter output power is exactly equal to the local load consumption. Therefore, the proposed method is to provide the reduction of the NDZ region close to zero. In all cases of the study, the islanding condition is successfully detected and the detection time is less than 40 ms. Only one input (voltage) signal is required in this technique, and the designed detection algorithm has computationally less burden on the DSP. Hence, the proposed method is computationally simple and fits well into PV inverter systems, and is suitable for online implementation in the actual system.

REFERENCES

[1] A. F. Robert and R. C. Dugan, “Distribution system analysis and the future smart grid,” *IEEE Trans. Ind. Appl.*, vol. 47, no. 6, pp. 2343–2350, Dec. 2011.

[2] W. Xiaoyu and W. Freitas, “Impact of positive-feedback anti-islanding methods on small-signal stability of inverter-based distributed generation,” *IEEE Trans. Energy Convers.*, vol. 23, no. 3, pp. 923–931, Sep. 2008.

[3] A. Eltawil Mohamed and Z. Zhengming, “Grid-connected photovoltaic power systems: Technical and potential problems—A review,” *Renewable Sustainable Energy Rev.*, vol. 14, no. 1, pp. 112–129, Jan. 2010.

[4] J. A. Laghari, H. Mokhlis, M. Karimi, A. H. A. Bakar, and H. Mohamad, “Computational intelligence based techniques for islanding detection of

distributed generation in distribution network: A review," *Energy Convers. Manag.*, vol. 88, pp. 139–152, Dec. 2014.

[5] *Test Procedure Islanding Prevention Measure Utility-Interconnected Photovoltaic Inverters*, IEC Standard 62116, 2008.

[6] *IEEE Recommended Practice Utility Interface Photovoltaic (PV) Systems*. IEEE Standard 929, Apr. 2000.

[7] *IEEE Standard for Interconnecting Distributed Resources With Electric Power Systems*, IEEE Standard 1547, Jul. 2003.

[8] D. Velasco, C. L. Trujillo, G. Garcerá, and E. Figueres, "Review of anti-islanding techniques in distributed generators," *Renewable Sustainable Energy Rev.*, vol. 14, no. 6, pp. 1608–1614, Aug. 2010.

[9] P. Mahat, Z. Chen, and B. Bak-Jensen, "Review of islanding detection methods for distributed generation," in *Proc. 3rd Int. Conf. Electr. Utility Deregulation Restructuring Power Technol.*, Apr. 6–9, 2008, pp. 2743–2748.

[10] Y. Zhihong, A. Kolwalkar, Y. Zhang, D. Pengwei, and R. Walling, "Evaluation of anti-islanding schemes based on non-detection zone concept," *IEEE Trans. Power Electron.*, vol. 19, no. 5, pp. 1171–1176, Sep. 2004.

[11] H. H. Zeineldin and J. L. Kirtley, "Performance of the OVP/UVP and OFP/UFP method with voltage and frequency dependent loads," *IEEE Trans. Power Del.*, vol. 24, no. 2, pp. 772–778, Mar. 2009.

[12] S.-I. Jang and K. H. Kim, "An islanding detection method for distributed generations using voltage unbalance and total harmonic distortion of current," *IEEE Trans. Power Del.*, vol. 19, no. 2, pp. 745–752, Apr. 2004.

[13] B. Singam and L. Y. Hui, "Assessing SMS and PJD schemes of anti-islanding with varying quality factor," in *Proc. IEEE Int. Power Energy Conf.*, Nov. 28–29, 2006, pp. 196–201.

[14] W. Freitas, X. Wilsun, C. M. Affonso, and H. Zhenyu, "Comparative analysis between ROCOF and vector surge relays for distributed generation applications," *IEEE Trans. Power Del.*, vol. 20, no. 2, pp. 1315–1324, Apr. 2005.

[15] A. Samui and S. R. Samantaray, "Assessment of ROCPAD relay for islanding detection in distributed generation," *IEEE Trans. Smart Grid*, vol. 2, no. 2, pp. 391–398, Jun. 2011.

[16] J.-H. Kim, J.-G.Kim, Y.-H. Ji, Y.-C. Jung, and C.-Y. Won, "An islanding detection method for a grid-connected system based on the Goertzel algorithm," *IEEE Trans. Power Electron.*, vol. 26, no. 4, pp. 1049–1055, Feb. 2011.

[17] H. Kazemi Karegar and B. Sobhani, "Wavelet transform method for islanding detection of wind turbines," *Renewable Energy*, vol. 38, no. 1, pp. 94–106, Feb. 2012.

[18] B. Matic-Cuka and M. Kezunovic, "Islanding detection for inverter-based distributed generation using support vector machine method," *IEEE Trans. Smart Grid*, vol. 5, no. 6, pp. 2676–2686, Nov. 2014.

[19] I. Y.-H. Gu and E. Styvaktakis, "Bridge the gap: Signal processing for power quality applications," *Electric Power Syst. Res.*, vol. 66, no. 1, pp. 83–96, Jul. 2003.

[20] N. W. A. Lidula and A. D. Rajapakse, "A pattern recognition approach for detecting power islands using transient signals—Part I: Design and implementation," *IEEE Trans. Power Del.*, vol. 25, no. 4, pp. 3070–3077, Oct. 2010.

[21] Y. Fayyad and A. Osman, "Neuro-wavelet based islanding detection technique," in *Proc. IEEE Elect. Power Energy Conf.*, Aug. 25–27, 2010, pp. 1–6.

[22] A. Pigazo, M. Liserre, R. A. Mastromauro, V. M. Moreno, and A. Dell'Aquila, "Wavelet-based islanding detection in grid-connected PV systems," *IEEE Trans. Ind. Electron.*, vol. 56, no. 11, pp. 4445–4455, Nov. 2009.

[23] M. Hanif, M. Basu, and K. Gaughan, "Development of EN50438 compliant wavelet-based islanding detection technique for three-phase static distributed generation systems," *IET Renewable Power Gener.*, vol. 6, no. 4, pp. 289–301, Jul. 2012.

[24] S. Alshareef, S. Talwar, and W. G. Morsi, "A new approach based on wavelet design and machine learning for islanding detection of distributed generation," *IEEE Trans. Smart Grid*, vol. 5, no. 4, pp. 1575–1583, Jul. 2014.

[25] J. Barros and R. I. Diego, "Application of the wavelet-packet transform to the estimation of harmonic groups in current and voltage waveforms," *IEEE Trans. Power Del.*, vol. 21, no. 1, pp. 533–535, Jan. 2006.

[26] J. Barros and R. I. Diego, "Analysis of harmonics in power systems using the wavelet-packet transform," *IEEE Trans. Instrum. Meas.*, vol. 57, no. 1, pp. 63–69, Jan. 2008.

[27] S. A. Saleh, A. S. Aljankawey, R. Meng, J. Meng, C. P. Diduch, and L. Chang, "Anti-islanding protection based on signatures extracted from the instantaneous apparent power," *IEEE Trans. Power Electron.*, vol. 29, no. 11, pp. 5872–5891, Nov. 2014.

[28] Q. He, "Vibration signal classification by wavelet packet energy flow manifold learning," *J. Sound Vibration*, vol. 332, no. 7, pp. 1881–1894, Apr. 2013.

[29] J. H. R. Enslinand Peter and J. M. Heskes, "Harmonic interaction between a large number of distributed power inverters and the distribution network," *IEEE Trans. Power Electron.*, vol. 19, no. 6, pp. 1586–1593, Nov. 2004.

[30] C. A. G. Marques, M. V. Ribeiro, C. A. Duque, P. F. Ribeiro, and E. A. B. Da Silva, "A controlled filtering method for estimating harmonics of off-nominal frequencies," *IEEE Trans. Smart Grid*, vol. 3, no. 1, pp. 38–49, Mar. 2012.

[31] W. Xiongfei, F. Blaabjerg, and W. Weimin, "Modeling and analysis of harmonic stability in an AC power-electronics-based power system," *IEEE Trans. Power Electron.*, vol. 29, no. 12, pp. 6421–6432, Dec. 2014.

[32] A. I. Megahed, A. Monem Moussa, H. B. Elrefaie, and Y. M. Marghany, "Selection of a suitable mother wavelet for analyzing power system fault transients," in *Proc. IEEE Power Energy Soc. General Meeting—Convers. Del. Electr. Energy*, Jul. 20–24, 2008, pp. 1–7.

[33] M. Heidari, G. Seifossadat, and M. Razaz, "Application of decision tree and discrete wavelet transform for an optimized intelligent-based islanding detection method in distributed systems with distributed generations," *Renewable Sustainable Energy Rev.*, vol. 27, pp. 525–532, Nov. 2013.

[34] S. R. Mohanty, N. Kishor, P. K. Ray, and J. P. S. Catalao, "Comparative study of advanced signal processing techniques for islanding detection in a hybrid distributed generation system," *IEEE Trans. Sustain. Energy*, vol. 6, no. 1, pp. 122–131, Jan. 2015.

[35] A. R. Oliva and J. C. Balda, "A PV dispersed generator: A power quality analysis within the IEEE 519," *IEEE Trans. Power Del.*, vol. 18, no. 2, pp. 525–530, Apr. 2003.

Hieu Thanh Do (S'14) was born in Hai Duong, Vietnam, in 1985. He received the B.S. degree in electrical engineering from the Hung Yen University of Technology and Education, Hung Yen, Vietnam, in 2008, and the M.S. degree in automation engineering from Le Quy Don University, Ha Noi, Vietnam, in 2010. He is currently working toward the Ph.D. degree in electric engineering and automation from the Hefei University of Technology, Hefei, China.

From 2009 to 2012, he was a Lecturer with the Hung Yen University of Technology and Education. His current research interests include renewable energy conversion and power electronic converters.

Xing Zhang (M'13–SM'14) was born in Shanghai, China, in 1963. He received the B.S., M.S., and Ph.D. degrees in electric engineering and automation from the Hefei University of Technology, Hefei, China, in 1984, 1990, and 2003, respectively.

Since 1984, he has been a Faculty Member of the School of Electric Engineering and Automation, Hefei University of Technology, where he is currently a Professor and is also with the Photovoltaic Engineering Research Center of Ministry of Education. His main research interests include photovoltaic generation technologies, wind power generation technologies, and distributed generation system.

Ngu Viet Nguyen received the B.S. degree in electrical engineering and the M.S. degree in electrical technology from the Hanoi University of Agriculture, Hanoi, Vietnam, in 2001 and 2007, respectively, and the Ph.D. degree in power system and its automation from Hohai University, Nanjing, China, in 2013.

He is currently a Doctor at the Department of Electrical and Electronic Engineering, Hung Yen University of Technology and Education, Hung Yen, Vietnam. His research interests include power system and its automation, as well as solar energy systems.

Shan Shou Li was born in Anhui, China, in 1979. He received the B.S. degree in electrical and information engineering from Anhui Jianzhu University, Hefei, China, in 2001, and the M.S. degree in electric engineering and automation from the Hefei University of Technology, Hefei, in 2007, where he is currently working toward the Ph.D. degree.

His research interests mainly focus on mismatch problem in the photovoltaic generation system.

Tho Thi-Thanh Chu was born in Nghe An, Vietnam, in 1985. She received the B.S. degree in electrical engineering from the Hung Yen University of Technology and Education, Hung Yen, Vietnam, in 2008, and the M.S. degree in automation engineering from Le Quy Don University, Ha Noi, Vietnam, in 2010.

Since 2009, she has been a Lecturer with the Hung Yen University of Technology and Education. Her current research interests include control systems and its automation.